

FOSSIL SHELL IN 3C 84 AS TEV γ -RAY EMITTER AND COSMIC-RAY ACCELERATOR

M. KINO^{1,2}, H. ITO³, K. WAJIMA¹, N. KAWAKATU⁴, H. NAGAI², R. ITOH⁵

Draft version February 7, 2018

ABSTRACT

We explore physical properties of the shocked external medium (i.e., a shell) in 3C 84 associated with the recurrent radio lobe born around 1960. In the previous work of Ito et al., we investigated a dynamical and radiative evolution of such a shell after the central engine stops the jet launching and we found that a fossil shell emission overwhelms that of the rapidly fading radio lobe. We apply this model to 3C 84 and find the followings: (i) The fossil shell made of shocked diffuse ambient matter with the number density of 0.3 cm^{-3} radiates bright Inverse-Compton (IC) emission with the seed photons of the radio emission from the central compact region and the IC emission is above the sensitivity threshold of the Cherenkov Telescope Array (CTA). (ii) When the fossil shell is produced in a geometrically thick ionized plasma with the number density of 10^3 cm^{-3} and the field strength in the shell may reach about 17 mG in the presence of magnetic fields amplification and the radio emission becomes comparable to the sensitivity of deep imaging VLBI observations. A possible production of ultra high energy cosmic-rays (UHECRs) in the dense shocked plasma is also argued.

Subject headings: galaxies: active radio continuum: galaxies gamma rays: galaxies galaxies: individual (3C 84, NGC 1275)

1. INTRODUCTION

Radio-loud active galactic nuclei (AGNs) are among the most powerful objects in the Universe. Interactions between jets and ambient medium drive strong collisionless shocks in the surrounding external medium. Therefore, AGN jets can provide us with a great variety of important information about fundamental physical processes in collisionless shocks (e.g., Marcowith et al. 2016 for a review). An AGN jet is thought to play an important role for radio-mode feedback against interstellar matter in its host galaxy (e.g., Fabian 2012 for review). According to the standard picture of jets in AGNs (e.g., Begelman et al. 1984), a jet is enveloped in a cocoon consisting of shocked jet material. The hot cocoon's pressure drives the forward shocks and the forward-shocked external medium produces the shell structure. Although the shell is a fundamental ingredient, physical properties of the shell have not been well studied because they are faint radio-quiet emitters (Carilli et al. 1988) and still undetected at radio wavelengths.

Recent theoretical work on forward shocks have provided us with basic properties of forward shocks in AGNs such as predicted high energy γ -ray emission (e.g., Fujita et al. 2007; Ito et al. 2011; Kino et al. 2013; Ito et al. 2015 (hereafter I15)), possible cosmic-ray production and magnetic field amplification (e.g., Berezhko 2008). However, comparisons between these theoretical predictions and observations are poorly studied because of the

paucity of information about the surrounding external medium in which forward shocks are driven.

The compact radio source 3C 84 (also known as NGC1275) is one of the nearby ($z = 0.018$) best-studied radio galaxies. 3C 84 shows intermittent jet activity (e.g., Nagai et al. 2010). Once the jet activity stops, the radio emission of the lobes fades out rapidly making the shell dominate the radio emission (I15). For this reason, the intermittent radio activity observed in 3C 84 makes this source a good candidate for observational studying the shell emission. Comparison between model spectra and observed non-thermal emission generally provides us with straightforward limits of magnetic fields (hereafter B -fields) strength and number density, particle (electron) acceleration efficiency in the shell.

The goal of this paper is to explore basic properties of the fossil shell in 3C 84 and its detectability. We will examine whether we can constrain the magnetic field strength and particle acceleration efficiency in the shell by comparing the theoretical predictions with the observations.

The layout of this paper is as follows. In §2, we briefly review the model following the work of I15. In §3, physical quantities associated with 3C 84 radio lobe and surrounding environment are summarized. In §4, the shell emission spectra predicted by applying the model to 3C 84 using the quantities shown in §3. Summary is presented in §5. In this work, we define the radio spectral index α_R as $S_\nu \propto \nu^{-\alpha_R}$. The cosmological parameters used here are as follows; $H_0 = 71 \text{ km/s/Mpc}$, $\Omega_\lambda = 0.73$ and $\Omega_m = 0.27$ (e.g., Komatsu et al. 2011). The redshift of 3C 84 ($z = 0.018$) is located at the luminosity distance $D_L = 75 \text{ Mpc}$ and it corresponds to 0.35 pc mas^{-1} .

2. MODEL

Details of the model of pressure-driven expanding jet-remnant system have already been well established (Ostriker & McKee 1988; I15 and references therein). In this

kino@kasi.re.kr

¹Korea Astronomy and Space Science Institute, 776 Daedeokdae-ro, Yuseong-gu, Daejeon 34055, Republic of Korea

²National Astronomical Observatory of Japan 2-21-1 Osawa, Mitaka, Tokyo, 181-8588, Japan

³Astrophysical Big Bang Laboratory, RIKEN, Saitama 351-0198, Japan

⁴National Institute of Technology, Kure College, 2-2-11 Agaminami, Kure, Hiroshima, 737-8506, Japan

⁵Department of Physics, Tokyo Institute of Technology, 2-12-1 Ohokayama, Meguro, Tokyo 152-8551, Japan

paper, we simply follow it in the present work.

In Figure 1, we take the specific case of 3C 84. The kinetic energy of the jets is dissipated via the termination shock at the hot spots and deposited into the cocoon (radio lobes) with its radius R and the shell with its width δR . In the present work, we estimate $R_{\parallel} \approx 10$ pc in 2015 (see Table 1). The cocoon is inflated by its internal energy. The cocoon drives the forward shock propagating in the external medium and the forward-shocked region is identical to the shell. The C3 component near the nucleus is the well-known newborn component (hot spot/radio lobe) which propagates southward (Nagai et al. 2010; Suzuki et al. 2012). O’Dea et al. (1984) and Walker et al. (2000) clarified the existence of dense ionized gas which causes FFA of northern jet. In this picture, we describe the dense gas as a ” plasma torus” which is suggested in some of radio galaxies (e.g., Kameno et al. 2001 for NGC 1052). Since the actual jet axis viewing angle is not 90 degrees, the northern part of the jet and radio lobe are hidden by FFA due to the surrounding matter (Walker et al. 2000). In Figure 1, the surrounding matter is described as the ionized plasma torus. The outside of the plasma torus would match a dust torus region. Since a geometrical relation between the dust torus and the ionized plasma torus is highly uncertain and it is still under debate (e.g., Netzer & Laor 1993; Czerny & Hryniewicz2011), we do not display the dust torus in Figure 1.

2.1. Dynamics

Here we briefly summarize the dynamics of the expanding cocoon. The cocoon radius (R) is determined by the momentum balance between the cocoon’s internal pressure and the ram pressure. The mass density of surrounding external matter (ρ_{ext}) at R is defined as

$$\rho_{\text{ext}}(R) = \rho_0 \left(\frac{R}{R_0} \right)^{-\alpha}, \quad (1)$$

where ρ_0 , R_0 , and α are the reference mass density, the reference radius, and the power-law index of ρ_{ext} , respectively. The shell width (δR) at R satisfies the relation $\delta R = (\hat{\gamma}_{\text{ext}} - 1)[(\hat{\gamma}_{\text{ext}} + 1)(3 - \alpha)]^{-1}R$, where $\hat{\gamma}_{\text{ext}}$ is the specific heat ratio of the external medium.

Following the previous work of I15, we consider two phases depending on the source age (t):

- (i) the phase in which the jet energy injection into the cocoon continues ($t < t_j$)
- (ii) the phase after the jet has switched off ($t > t_j$)

where t_j denotes the duration of the jet injection. Hereafter, we assume that the kinetic power of the jet (L_j) is constant in time when $t < t_j$ and $L_j = 0$ for $t \geq t_j$. The bulk kinetic energy of the jet is dissipated and deposited as the internal energy of the cocoon and shell. As for the early phase with jet energy injection into the cocoon, the time evolution of R is given by

$$R(t) = CR_0^{\frac{\alpha}{5-\alpha}} \left(\frac{L_j}{\rho_0} \right)^{\frac{1}{5-\alpha}} t^{\frac{3}{5-\alpha}} \quad (t < t_j), \quad (2)$$

where C is the numerical coefficient and the explicit form of C is shown in I15. Note that L_j/ρ_0 is the key control

parameter which governs the dynamical expansion of the bubble (Kawakatu et al. 2009a and reference therein).

After the energy injection from the jet stops, (i.e., $t > t_j$) the cocoon will rapidly lose its energy due to adiabatic expansion and give away most of its energy into the shell within a dynamical timescale. Hence, after $t \approx t_j$, the cocoon pressure becomes dynamically unimportant, and the energy of the shell becomes dominant. Therefore, the behavior of the cocoon asymptotically follows the Sedov-Taylor expansion and the expansion velocity is given by

$$v(t) = \dot{R}(t) \propto t^{-(3-\alpha)/(5-\alpha)} \quad (t > t_j). \quad (3)$$

During the Sedov-Taylor expansion phase, the adiabatic relation $P_c V_c^{\hat{\gamma}_c} = \text{const}$ holds where P_c , V_c , and $\hat{\gamma}_c$ are the pressure, volume, and the specific heat ratio of the cocoon, respectively. Then, we can approximately describe $R_c(t)$ as follows:

$$R_c(t) = R(t_j) \left[\frac{P_c(t_j)}{P_c(t)} \right]^{1/3\hat{\gamma}_c} \quad (t > t_j). \quad (4)$$

Note that the cocoon expands slower than the propagation speed of the forward shock and the shell width correspondingly becomes slightly wider (e.g., Figure 1 of Reynolds & Begelman 1997). This behavior holds also for relativistic regime and it is known as an expanding-coasting phase (e.g., Piran 1999 for a review.) The time evolution of P is given by

$$P_c(t) \approx P_{\text{shell}}(t) = \frac{3}{4}\rho_0 \dot{R}(t)^2 \left[\frac{R(t)}{R_0} \right]^{-\alpha} \quad (t > t_j), \quad (5)$$

by matching the pressures between the shell and cocoon at $t = t_j$. For the shock jump condition between the shell and external medium, the specific heat ratio of external medium is set as $5/3$ and it leads to $\delta R/R = 1/12$.

Hereafter, the subscripts \parallel and \perp are used for R and v (see Figure 1). The subscript \parallel describes the direction parallel to the jet axis, while the subscript \perp corresponds to the direction perpendicular to it.

2.2. Geometry of external medium

Various radio observations of 3C 84 suggest the existence of dense external ionized gas (i.e., plasma) in the central region (e.g., O’Dea et al. 1984; Walker et al. 2000; Plambeck et al. 2014). This circum-nuclear structure of dense ionized gas hides the northern radio lobe via free-free absorption (FFA) process (Walker et al. 2000). Hence, shocks driven by the cocoon propagate through both the diffuse ambient medium and the dense circum-nuclear structure of ionized gas. Geometry of the dense plasma is quite uncertain. If the dense plasma is a geometrically thin disk, then the volume of the shocked dense plasma may be negligibly small. On the other hand, if the plasma shows a torus-like geometry, the volume would not be that small. We introduce a free parameter which represents filling factors of the shocked plasma torus and ambient matter over the shell as f_{torus} and f_{amb} . Since the cocoon expands quasi-spherically in all directions, $f_{\text{amb}} + f_{\text{torus}} \approx 1$ holds where $0 < f_{\text{amb}} \lesssim 1$, and $0 \lesssim f_{\text{torus}} < 1$.

In the present work, we examine the case when the dense plasma has the torus-like geometry (Figure 1). In

the present work, we examine the case in which $f_{\text{amb}} \approx f_{\text{torus}} \approx 0.5$ is realized.

2.3. Non-thermal emission

Since the details have been already explained in Kino et al. (2013) and I15, here we briefly review the basic treatment of non-thermal electrons and photons in a shell. We solve the kinetic equation of the non-thermal electrons including the back reaction of radiative and adiabatic coolings. First, as for the external photon field against IC process we consider (1) UV photons from a standard accretion disk, (2) IR photons from a dust torus, (3) synchrotron photons from the fading radio lobe, (4) synchrotron photons from the central compact region, and (5) synchrotron photons from the shell. Second, we include the effect of absorption via $\gamma\gamma$ interaction. Very high-energy (VHE) photons suffer from absorption via interaction with various soft photons (e.g., Coppi & Aharonian 1997). Here, we include the $\gamma\gamma$ absorption due to photons intrinsic to the source and photons from the extragalactic background light (EBL). The absorption opacity with respect to the intrinsic photons can be calculated by summing up all of the photons from (1) the shell, (2) the radio lobes, (3) the dusty torus, and (4) the accretion disk and we multiply the $\gamma\gamma$ absorption factor of $\exp(-\tau_{\gamma\gamma})$ with the unabsorbed flux. For simplicity, we deal with the absorption effect at the first order and we neglect cascading effect. For the cosmic $\gamma\gamma$ opacity, we adopt the standard model of Franceschini et al. (2008).

3. PHYSICAL QUANTITIES IN 3C 84

In this section, we discuss physical parameters of 3C 84. All of the quantities are summarized in Table 1.

3.1. Total power of the jet : L_j

The mass of the black hole in NGC 1275 is estimated to be around $M_{\odot} \approx 8 \times 10^8 M_{\odot}$ by gas kinematics (Schawachter et al. 2013). Correspondingly, the Eddington luminosity of NGC 1275 is $L_{\text{Edd}} \approx 1 \times 10^{47} \text{ erg s}^{-1}$. It is natural to suppose that the total power of the jet (L_j) satisfies the relation of $L_{\text{Edd}} \geq L_j$ ⁶.

Various estimates of the total power of the jet in 3C 84 at the central parsec region may be found in the literature. Heinz et al. (1998) argued that the time-averaged total power of the jet in NGC 1275 probably exceeds $L_j \sim 10^{46} \text{ erg s}^{-1}$. They derived the conclusion based on the observed properties of X-ray cavities in the central region of the Perseus cluster, which is supposed to be inflated by relativistic particles of the shocked jet. They also suggested that the jet power in a quiescent state (corresponding to off-state mentioned in the paper of Reynolds and Begelman 1997) may be lower than $\sim 10^{46} \text{ erg s}^{-1}$. Such a quiescent state case would correspond to the estimate of the power $L_j \sim 5 \times 10^{44} \text{ erg s}^{-1}$ in Abdo et al. (2009). The observed luminosity at each energy band is of order of $\sim 10^{43} \text{ erg s}^{-1}$ from radio to GeV γ -ray band (Abdo et al. 2009). Therefore, the bolometric luminosity is estimated to be $\sim 10^{44} \text{ erg s}^{-1}$. Hence, a typical case of radiative efficiency of non thermal electrons with a few percent results in the electron

kinetic power of the order of a few $\times 10^{45} \text{ erg s}^{-1}$. The proton component is also supposed to contribute to the total jet power. It is quite reasonable that L_j corresponds to a few percent of L_{Edd} . These estimates are consistent with a jet luminosity of the order of a few $\times 10^{45} \text{ erg s}^{-1}$, in agreement with the range of values reported in the literature. Therefore, following Heinz et al. (1998), we adopt $L_j = 5 \times 10^{45} \text{ erg s}^{-1}$ (i.e., 5% of the Eddington power) as a fiducial value.

3.2. Fading radio lobe

In the present work, we will focus on VLBA data at 15 GHz because there are sufficient archival data (MOJAVE project summarized by Lister et al. 2009, see also <http://www.physics.purdue.edu/MOJAVE/>) that enable us to explore basic properties of 3C 84 in detail and the spatial resolution is suitable for exploring shells.

3.2.1. VLBA images of fading radio lobe at 15 GHz

In order to see basic characteristics of the radio lobe, we analyzed three epochs of relatively good quality VLBA archival data of 3C 84 at 15 GHz obtained in 1994, 2010, and 2015 (the project ID are BR003, BL149CX, and BL193AS, respectively). Two of them are adopted from MOJAVE data (<http://www.physics.purdue.edu/MOJAVE/>). The initial data calibration was performed with the Astronomical Image Processing System (AIPS) developed at the National Radio Astronomy Observatory. First, a priori amplitude calibration was applied using the measured system noise temperature and the elevation-gain curve of each antenna. We then calibrated the amplitude part of bandpass characteristics at each station using the auto-correlation data. We applied opacity correction due to the atmospheric attenuation, assuming that the time variation of the opacity is not significant during each observation. The visibility phase and delay offset between different sub-bands were solved by using 3C 84 itself. Fringe fitting was performed with the AIPS task "fring" on 3C 84 by averaging over all the IFs. Imaging and self-calibration were performed using the Difmap software package (Shepherd 1997). The final images were produced after iterations of CLEAN, phase, and amplitude self-calibration processes. We used a natural weighting scheme.

In Figure 2, we show the obtained intensity map of the fading radio lobe. The image root-mean-square (rms) of VLBA at 15 GHz in Figure 2 of each three epochs (1σ) is, 18.5 mJy/beam (1994, ID BR003), 3.1 mJy/beam (2010, ID BL149CX), and 3.0 mJy/beam (2015, ID BL193AS), respectively. The high rms and large beam size for the observation performed in 1994 (ID BR003) is due to problems at the SC station which cause the flagging of the data from that antenna. The total flux of the fading lobe in each epoch is shown in the figure caption. We define the source radius R as the de-projected distance between the nucleus (C1 component) to the head of the radio lobe and it is a measured quantity. The projected angular distance is about 20 mas. The allowed de-projection distance is $R_{\parallel} \approx 9 - 16 \text{ pc}$ based on the previous estimate of the jet viewing angle $\theta_{\text{view}} = 25^\circ$ and $\theta_{\text{view}} = 49^\circ$ derived by Tavecchio et al. (2014) and Fujita and Nagai (2017), respectively. At the center of

⁶ see however Ghisellini et al. (2014)

each epoch, the bright central compact region consists of three sub-components: C1, likely hosting the source core, C2, a diffuse and faint component, and C3, a bright hot-spot-like component (see e.g., Nagai et al. 2010). The central region accounts for the majority of the source emission and its synchrotron photons play a dominant role as seed photons for IC scattering in the shell.

The long-term radio light curve of 3C 84 at 8 GHz shows the flux density increase started around 1960 (Nesterov et al. 1995). Therefore, the age of the dying radio lobe in 3C 84 is estimated as $t \sim 50 - 60$ years in 2015. In this work, we set $t = 55$ years.

3.2.2. on the duration of the jet injection

It is hard to estimate the duration of the jet injection (t_j) or equivalently the time when the jet stopped accurately, because it is not a direct observable. At least, the fading of the radio lobe clearly indicates that t_j is shorter than t . In this work, we will examine the three cases of $t - t_j = 5, 10,$ and 30 years.

3.3. Shell

Once we know the evolution of fading radio lobe, then we can derive the advancing velocities of the shell.

3.3.1. Advancing velocity parallel to the jet: v_{\parallel}

The advancing velocity of the radio lobe head (v_{\parallel}) has been well constrained in the literatures and we simply follow it. In Asada et al. (2006), the authors measure it with the two epoch data (1998 August and 2001 August) of VSOP observations at 5 GHz and derived an advancing velocity as $v_{\parallel} \sim 0.5 c$. Lister et al. (2013) derived $v_{\parallel} \sim 0.3c$ in the framework of MOJAVE project. The lobe advancing velocity seen in Figure 2 is consistent with these v_{\parallel} in the literature.

3.3.2. Advancing velocity parallel to the jet: v_{\perp}

On the contrary to v_{\parallel} , little is known about propagation velocity of the shell perpendicular to the jet axis (v_{\perp}), since there is no observational constraint on the high- n shell. In our model, same amount of internal energy is allocated the shocked torus and shocked ambient matter regions. Therefore, the pressure in the shocked torus is larger than that in the shocked ambient matter region because of the smaller volume.

The propagation speed of v_{\perp} is governed by the balance between the ram pressure and the cocoon pressure in the perpendicular direction, i.e., $\rho_{\text{ext}} v_{\perp}^2 \propto P_{c,\perp}$ where $P_{c,\perp}$ is the pressure in the region behind the high- n shell (see Figure 1). The larger ρ_{ext} leads to (1) the smaller v_{\perp} and correspondingly (2) the smaller radius for the region behind the high- n shell (R_{\perp}). Then, the pressure $P_{c,\perp}$ plays an important role for determining v_{\perp} because $P_{c,\perp} \propto E_{c,\perp}/V_{c,\perp} \propto R_{\perp}^{-2}$ where $V_{c,\perp} \propto R_{\perp}^3$ and $E_{c,\perp} \propto R_{\perp}$. The smaller R_{\perp} leads to the larger $P_{c,\perp}$. Therefore, the larger ρ_{ext} in the high- n shell and the larger $P_{c,\perp}$ are in the high- n shell largely cancelled each other out. Then, v_{\perp} does not slow down significantly. With the model parameters in the present study summarized in Table 1, we can obtain $v_{\perp}/v_{\parallel} \approx R_{\perp}/R_{\parallel} \approx 1/5$ for $t = 55$ years.

3.3.3. Magnetic fields strength: B_{shell}

Here we argue the viable range of magnetic field strength. First, we argue the lower limit of magnetic field strength averaged over the spatial scale ~ 100 pc. Silver et al. (1998) discovered the extended radio halo structure at 330 MHz (hereafter we call "milli-halo" according to their original naming) with its averaged diameter of ~ 500 mas which is slightly elongated along the orientation of the jet axis. Furthermore, the milli-halo has a brightness temperature $\sim 3 \times 10^7$ K, it is surely non thermal. Thus the emission most probably originated in the jet remnant generated by the past activity of the central engine. Then Silver et al. (1998) estimate the magnetic field strength in the milli-halo as $B_{\text{ext}} \approx 200 \mu\text{G}$ by assuming equipartition condition together with the path length of 75 pc. Taylor et al. (2006) estimated the field strength in the central region (< 2 kpc) of the Perseus cluster by using the equipartition assumption between the magnetic field and hot plasma which emit X-ray with a temperature of 5×10^7 K and number density $\sim 0.3 \text{ cm}^{-3}$ and have obtained $B_{\text{ext}} \approx 300 \mu\text{G}$ which is comparable to the estimate obtained by Silver et al. (1998). Taylor et al. (2006) further estimated the field strength within the 10 pc scale radio lobe as by measuring the rotation measure (RM) associated with the lobe's tip, which can be regarded as the hotspot. The measured value shows $RM \sim 7 \times 10^3 \text{ rad m}^{-2}$. By adopting the path length as 1 pc, they derived the value of $B_{\text{ext}} \approx 50 \mu\text{G}$. Based on these previous works, here we set the fiducial magnetic field strength in the shell as $B_{\text{shell}} \approx 0.1 \text{ mG}$.

3.4. External medium

Hereafter, we denote the number density of external medium as n_{ext} . We assume that the external medium consists of both a diffuse gas with low number density (n_{amb}) surrounding the radio source, and a circum-nuclear structure, e.g. a torus, of dense ionized gas (n_{torus}). A sketch is shown in Figure 1.

3.4.1. Number density of diffuse ambient medium: n_{amb}

Taylor et al. (2006) estimated the number density by using the deep Chandra observation (Fabian et al. 2006). Within the central 0.8kpc, the density profile is severely affected by the nucleus. So, they estimated an average central density over the inner 2kpc to be $n_{\text{amb}} \sim 0.3 \text{ cm}^{-3}$. Regarding the upper limit of number density we adopt the value recently obtained by Fujita et al. (2016). They make two assumptions that (1) hot gas outside the Bondi radius is in nearly a hydrostatic equilibrium in a gravitational potential, and (2) the gas temperature near the galaxy centre is close to the virial temperature of the galaxy. Then, they obtain $n_{\text{amb}} \sim 10 \text{ cm}^{-3}$ in the inner part of Perseus cluster. Then we obtain $0.3 \text{ cm}^{-3} \leq n_{\text{amb}} \leq 10 \text{ cm}^{-3}$ by regarding the value derived by Fujita et al. (2016) as the upper limit of n_{amb} . In this work, we set $n_{\text{amb}} \approx 0.3 \text{ cm}^{-3}$ as a fiducial one based on Fabian et al. (2006).

3.4.2. Number density of plasma torus: n_{torus}

The existence of dense thermal gas surrounding 3C 84 was discovered by O'dea et al. (1984). They suggested that 3C 84 is embedded in a dense thermal gas with the number density $\sim 2 \times 10^3 \text{ cm}^{-3}$ derived from the condition of depolarization by differential Faraday rotation

in the external plasma. Walker et al. (2000) also confirm that the spectra are consistent with FFA by VLBA observations at 5, 8, 15, and 22 GHz and the northern radio lobe feature is on the far side of the system relative to the Earth. Therefore, the size of the plasma (ionized gas) should be spatially extended to the scale at least comparable to the radio lobe seen in Figure 2 since the northern lobe is still hidden by the FFA.

Although the geometrical details of the thermal gas are highly uncertain, it is clear that the required total power of the jet would be very large if the dense thermal gas with $\sim 10^3 \text{ cm}^{-3}$ completely envelopes the overall 3C 84 system. For this reason, we regard it as the dense ambient matter and as a geometrically thick plasma torus. Here, we set $n_{\text{torus}} = 1 \times 10^3 \text{ cm}^{-3}$ with the path length of about 10 pc which is comparable to R (see the next sub-sections.)

3.5. External photon field

3.5.1. Synchrotron emission from the central compact region

As already explained, it is well known that the central compact region consists of three sub-components: C1, likely hosting the source core, C2, a diffuse and faint component, and C3, a bright hot-spot-like component. Hereafter, synchrotron photons coming from the whole central component region are considered, with no distinction among those sub-components. This should make the method and results of this work easier and clearer to read and follow.

In Figure 3, we show the recent image of the central compact region with KaVA at 43 GHz. KaVA is a combined VLBI array with KVN (Korean VLBI Network) and VERA (VLBI Exploration of Radio Astrometry) operated by KASI and NAOJ, respectively and its baseline lengths range from 305 to 2270 km (see Niinuma et al. 2014 for details). This is one of the epochs of a long-term KaVA monitoring of 3C 84 at 43GHz (<http://radio.kasi.re.kr/kava/>) and we conducted a data reduction in a standard way, already described in sub-section 3.2.1. The obtained total flux of the central compact region at 43 GHz is about 15 Jy in 2015 and thus we obtain $L_{43G} = 4\pi D_L^2 S_{\nu\nu} \approx 4 \times 10^{42} \text{ erg s}^{-1}$. The measured total flux density of the central compact region is consistent with the one obtained by the blazar monitoring project led by Boston university group (<https://www.bu.edu/blazars/VLBAproject.html>).

The long term VLBI monitoring of the central compact region at 22 GHz shows a gradual monotonic increase of the flux from ~ 2006 (Nagai et al. 2010, 2012; Suzuki et al. 2012; Chida et al. 2015). The total flux of the central compact region at 14mm measured by VERA is ~ 20 Jy and from this we obtain $L_{22G} = 4\pi D_L^2 S_{\nu\nu} \approx 3 \times 10^{42} \text{ erg s}^{-1}$. In the present work, we set an averaged spectral index as $\alpha_R \approx 0.3$ in S_{ν} of the central compact region (Chida et al. 2015). In §4, we will find that the synchrotron photons from the central compact region are the dominant seed photons for the IC scattering.

3.5.2. Synchrotron emission from the fading radio lobe

Synchrotron photons from the fading radio lobe are also regarded as seed photons for IC in the shell although it does not play a dominant role. As shown in Figure 2, the total fluxes of the fading radio lobes at 15 GHz are

7.4, 2.0, 1.2 Jy in 1994, 2010 and 2015, respectively. Then the corresponding luminosity of the fading radio lobe in 2015 is $L_{\text{lobe}} \approx 1 \times 10^{41} \text{ erg s}^{-1}$ and it is shown in Table 1. In §4, the synchrotron photons from the fading radio lobe will turn out to be less dominant as seed photons for the IC scattering.

3.5.3. Thermal emission from accretion disk and dust torus

Here we estimate accretion disc luminosity (L_{UV}) in 3C 84 using the observed line spectra. Using the observation data obtained by Kanata telescopes HOWPol (Hiroshima One-shot Wide-field Polarimeter) (Kawabata et al. 2008), Yamazaki et al. (2013) addressed the variation of the line ratio of $(\text{H } \alpha + [\text{NII}]) / [\text{OII}]$ which reflects the activity of UV photons from accretion disc. The broad H α line shows no significant variability during 2010-2011. Although there is a possibility of a long-term (~ 10 year scale) change of the activity of the accretion disk, here we estimate L_{UV} by regarding the flux obtained by Kanata as a conservative minimum value. Using the same data, we further revisited and evaluated the line spectra in 3C 84 and we estimate the UV luminosity as follows (Kino et al. 2016). The [OII] luminosity is derived as $L_{[\text{OII}]} = 1.9 \times 10^{42} \text{ erg s}^{-1}$ by Ho et al. (1997), while the H alpha plus [NII] line luminosity measured by KANATA HowPOL is $L_{\text{H}\alpha + [\text{NII}]} = 1.2 \times 10^{42} \text{ erg s}^{-1}$. According to Ho et al. (1997), $L_{[\text{NII}]}$ typically contributes to $L_{\text{H}\alpha + [\text{NII}]}$ up to $\sim 20\%$. Adopting the value of [OI] luminosity from Ho et al. (1997) and the empirical relation by Greene and Ho (2005), we obtain $L_{UV} \approx 5 \times 10^{42} \text{ erg s}^{-1}$.⁷ In addition, the luminosity ratio of $L_{\text{bol}} / L_{\text{Edd}} \sim 4 \times 10^{-3}$ where L_{bol} is the bolometric luminosity of 3C 84 (e.g., Levinson et al. 1995 and reference therein). Thus, the classification of the accretion flow in 3C 84 may settle down on the border between the standard Shakura-Sunyaev disk (Shakura and Sunyaev 1973) and Radiatively Inefficient Accretion Flow (RIAF). In the present work, however, we do not take the RIAF emission into account because it is negligibly small as seed photons for IC at the fossil shell.

The dust emission at the center of NGC 1275 has been investigated with *Herschel* data by Mittal et al. (2012) and they derived the total dust luminosity as $L_{\text{IR, total}} \sim 5 \times 10^{44} \text{ erg s}^{-1}$. spatially-ntegrated over arcsec angular-size scale. Because of heavy absorption by dust torus in young compact radio sources (e.g., Kawakatu et al. 2009b; Ostorero et al. 2010), it is difficult to estimate the dust-torus luminosity accurately. Hence, we use the work of Calderone et al. (2012) to give us a better estimation of the dust torus luminosity (L_{IR}). Calderone et al. (2012) explore the fraction of torus re-emission of absorbed accretion disc radiation for about 4000 radio-quiet AGNs and they found that the dust torus reprocesses 1/3-1/2 of the accretion disk luminosity. Based on their work, we set $L_{\text{IR, torus}} = \frac{L_{UV}}{2}$. The lower value of $L_{\text{IR, torus}}$ compared to $L_{\text{IR, total}}$ obtained by Mittal et al. (2012) can be consistent with each other, since the spatial resolution of *Herschel* is much larger than the size of dust-torus (sub-arcsec scale) and it probably contains

⁷ Ho et al. (1997) did not explicitly mention the value of H_0 in their paper. If they adopted $H_0 = 50 \text{ km/s/Mpc}$, then they underestimated of line luminosities by a factor of ~ 2 .

galactic-dust emission.

4. PREDICTED SHELL SPECTRA

In the previous section, we carefully discuss the observed quantities of 3C 84 and the physical quantities in the model, which are summarized in Tables 1 and 2. Since 3C 84 is one of the best-studied radio sources, we have tight constraints of observational quantities. In this section, we show the non-thermal emission spectra from the fossil shell in 3C 84 after stopping the jet energy injection. Here, we conservatively set the total luminosity of the central compact region as constant in time. Since the central compact region still gets brighter, the resultant fossil shell spectra to be shown here would correspond to conservative lower limit cases.

As for treatment of fading radio lobes, we simply follow our previous work of I15. We set a large value of electron gyro-factor in the lobe as $\xi_{e,\text{lobe}} = 10^7$. In general, the gyro-factor is proportional to a particle acceleration timescale and thus it determines the maximum energy of those accelerated particles. Change of $\xi_{e,\text{lobe}}$ value has no impact on the results of this work. We set the power-law index of injected electrons in the lobe as $p_{e,\text{lobe}} = 2.2$ corresponding to the standard value for relativistic shocks (e.g., Bednarz & Ostrowski 1998; Achterberg et al. 2001; Kirk 2000). As for energetics, we simply assume the equipartition between B -fields and electrons i.e., $\epsilon_e = \epsilon_B \approx 0.1 - 0.01$. For avoiding complexity of the figures, we do not overlay the fading radio lobe spectra. We find that the IC emission due to the synchrotron seed photons from the fading lobe are not dominant in the fossil shell spectra.

We also note that an actual total emission from the fossil shell should be the sum of the high- n and low- n spectra. Below, we separately discuss the spectra from high- n and low- n for better clearness.

4.1. The case of $n_{\text{ext}} = n_{\text{amb}}$

In Figure 4, we show the emission spectrum from the shocked ambient medium (i.e., low- n shell). Following the physical parameters reported in Tables 1 and 2 and discussed in §3, we estimate the expected emission from the shell that is expanding in a low-density ambient medium, i.e., $n_{\text{amb}} = 0.3 \text{ cm}^{-3}$. The jet power, age, and the magnetic field strength in the shell are, respectively, $L_j = 5 \times 10^{45} \text{ erg s}^{-1}$, $t = 55 \text{ years}$ and $B_{\text{shell}} = 0.1 \text{ mG}$. By solving the evolution governed by Eq. (2) with these L_j , t and n_{amb} , we obtain $R_{\parallel} \approx 8 \text{ pc}$ which is similar to the minimum value of the estimated $R_{\parallel} \approx 9 \text{ pc}$. (Since a spherical symmetry is assumed Eq. (2) for simplicity, all of the jet power is isotropically ejected. Hence, a slightly smaller R_{\parallel} by the model is more consistent.) The corresponding advancing velocity of the shell is $v_{\perp} \sim 0.26 c$. In addition, we can readily find that a larger R_{\parallel} requires a fairly large L_j .

The shell spectrum is IC-cooling dominated and the IC peak occurs in the TeV γ -ray energy band. The IC component of synchrotron photons from the central compact region in Figure 2) is dominant in the shells. The distance from the seed photon source and the fossil shell is taken into account. Even though the distance from the central compact region and the fossil shell is about 10 pc and the photon energy density decrease as R^{-2} , the

IC component of the central compact region is still more dominant than the IC component of the fading radio lobe simply because the synchrotron luminosity of the central compact region is much higher than that from the fading lobe.

The predicted shell spectra have a trend similar to the ones shown in our previous work of I15. The opacity for $\gamma\gamma$ interaction between EBL and TeV photons is sufficiently small because of its proximity and we find that the predicted TeV γ -ray flux can be comparable to the sensitivity of CTA (<https://web.cta-observatory.org/science/cta-performance/>) with the integration time 50 hours. As reported in the Astronomer's telegram (<http://www.astronomerstelegram.org>), the data show variabilities in TeV γ -ray flux (e.g., Mirzoyan 2016, 2017; Mukherjee and VERITAS Collaboration 2016, 2017; Lucarelli et al. 2017; Ahnen et al. 2016). Such variabilities can be naturally explained by the emission from the blazar region (e.g., Tavecchio et al. 2014). On the other hand, the fossil-shell emission does not show such variabilities. Since the TeV γ -ray emission from a fossil-shell is less luminous than those from the blazar region, a low-activity phase of the blazar region is favored in search of the fossil shell emission.

It is well known that IC scattering process is divided into two regimes, i.e., Thomson and Compton regimes. Using the characteristic energy of the seed photons (E_{seed}) and electrons ($E_e = \gamma_e m_e c^2$), the following relation is satisfied

$$2E_{\text{seed}} \times E_e \begin{cases} \ll (m_e c^2)^2 & (\text{Thomson regime}) \\ \gtrsim (m_e c^2)^2 & (\text{Compton regime}). \end{cases} \quad (6)$$

The maximum energy of IC spectrum ($h\nu_{\text{IC,max}}$) in the case of the Thomson regime is given by

$$h\nu_{\text{IC,max}} \approx \gamma_{e,\text{max}}^2 E_{\text{seed}} \quad (\text{Thomson regime}), \quad (7)$$

while $h\nu_{\text{IC}}$ is written as

$$\begin{aligned} h\nu_{\text{IC,max}} &\approx \gamma_{e,\text{max}} m_e c^2 \\ &= E_{e,\text{max}} \quad (\text{Compton regime}), \end{aligned} \quad (8)$$

for the Compton regime. Keeping this in mind, let us argue which scattering regime is realized for seed photons considered in this work. Against UV photons with the energy E_{UV} from an accretion disk, the IC scattering is taken place in Compton regime for electrons with their energy

$$E_e \gtrsim \frac{(m_e c^2)^2}{2E_{\text{UV}}} \approx 12 \text{ GeV} \left(\frac{E_{\text{UV}}}{10 \text{ eV}} \right)^{-1}. \quad (9)$$

Thus we find that $h\nu_{\text{IC,max}}$ is significantly limited by the Klein-Nishina effect although $E_{e,\text{max}}/m_e c^2$ extends up to $\sim 10^{7.5}$ in this case. From this, we can easily understand that IC scattering against IR photons from dusty torus is also in the range of Compton regime. On the other hand, the seed photons from the central compact region with its characteristic energy E_{mm} is IC scattered in the Thomson regime and thus we obtain

$$h\nu_{\text{IC,max}} \approx 10^{12} \text{ eV} \left(\frac{\gamma_{e,\text{max}}}{10^{7.5}} \right)^2 \left(\frac{E_{\text{mm}}}{10^{-3} \text{ eV}} \right). \quad (10)$$

This well explains the IC spectra in Figure 4.

In Figure 5, we show the three epochs of the predicted shell spectra. As already explained in I15, the shell almost keeps its emission flux level because fresh electrons are continuously supplied into the shell via the forward shock driven by the cocoon/radio-lobes while the radio-lobes rapidly fade out without jet energy injection.

4.2. The case of $n_{\text{ext}} = n_{\text{torus}}$

4.2.1. The case with B -amplification

Here, we take the process non-linear amplification of the magnetic fields into account (Lucek & Bell 2000; Bell & Lucek 2001), although little attention has been paid in the research field of AGN jets so far. Based on Lucek & Bell, it is expected that cosmic ray (CR) streaming in AGN jets would drive large-amplitude Alfvén waves and the CR streaming energy is transferred to the perturbed magnetic field of the Alfvén waves. Let us discuss the case when B -amplification is effective in the torus region (i.e., $n_{\text{ext}} = n_{\text{torus}}$). In this work, following the pioneering work of Berezhko (2008) which first introduces nonlinear amplification process of the magnetic field in AGN jets into account, we employ the empirical relation of

$$\frac{B_{\text{shell}}^2}{8\pi} \approx 3 \times 10^{-3} \rho_{\text{torus}} v_{\perp}^2,$$

obtained by Berezhko (2008) where $\rho_{\text{torus}} = n_{\text{torus}} m_p$. Then, we conservatively obtain the maximum value of the high- n shell's field as

$$B_{\text{shell}} \lesssim 17 \text{ mG}, \quad (11)$$

where $n_{\text{torus}} = 1 \times 10^3 \text{ cm}^{-3}$ and $v_{\perp} \sim v_{\parallel}/5 \approx 0.05c$ are adopted here. This empirical relation by Berezhko (2008) is justified by recent studies of high-resolution Magnetohydrodynamical (MHD) simulations. In particular, turbulence can significantly amplify B -field (e.g., Giacalone & Jokipii 2007; Inoue et al. 2009; Guo et al. 2012; Sano et al. 2012; Fraschetti 2013; Ji et al. 2016). For instance, the amplification factor of B -fields obtained by Ji et al. (2016) indeed reaches over ~ 100 which is consistent with the value discussed here. Note that a pile-up process of the B -field lines as the jet propagates sweeping the field lines in the torus could also help B -fields amplification (Rocha da Silva et al. 2015).

In Figure 6, we present the resultant fossil-shell emission spectra of dense fossil shell when the amplified B -fields become $B_{\text{shell}} \sim 17 \text{ mG}$. The bump at 10^{20} Hz corresponds to thermal bremsstrahlung emission from the fossil-shell. The temperature and number density in the fossil-shell are determined by Rankine-Hugoniot conditions (see I15 for details). In radio band, a bright synchrotron emission from the dense fossil shell is predicted. Here we estimate a typical detection-limit against a high- n shell at 15 GHz for future VLBI observation. As already shown in Figure 2, the typical image rms is found as 3 mJy/beam . Here, the case of $7\text{-}\sigma$ detection is considered. A required number of the VLBA beam at 15 GHz which can fill the the shell-surface area on the sky plane can be approximately estimated as $[2\pi f_{\text{torus}} \times 4 \text{ mas}(4 \text{ mas} \frac{\delta R}{R})] / [((\pi/4)(0.7 \times 0.4) \text{ mas})] \sim 19$ where $20/5 = 4 \text{ mas}$ as the angular size of R_{\perp} , $f_{\text{torus}} = 1/2$ and $\delta R/R = 1/12$ are used.

Then we can get the typical detection-limit as $3 \text{ mJy/beam} \times 19 \text{ beam} \times 7\sigma \approx 2 \times 10^{-14} \text{ erg s}^{-1} \text{ cm}^{-2}$. By comparing this detection-limit and the predicted shell spectra, we can argue a detectability of the shell emission at 15 GHz . The predicted flux density is comparable with the detection-limit at 15 GHz . Therefore, performing deeper imaging observations of VLBA and/or other VLBI in the future will generally give us meaningful constraints on fossil shell model parameters. For example, a usage of High Sensitivity Array (HSA), which is VLBA together with the Green Bank Telescope, phased VLA, and Effelsberg (<https://science.nrao.edu/facilities/vlba/proposing/HSA>) would enable us to get better sensitivity by an order of magnitude and will increase the chance to detect the fossil shell emission in 3C 84.

It is worth mentioning that the detectability of the shell might be limited not by the image thermal noise but the dynamic range. In such a case, better uv-coverage is essential for the detection. The total flux of the central compact region is about $\sim 10 \text{ Jy}$ level with a year-scale increase. Then, the required dynamic range is about a few times of 1000 if the flux density of the fossil shell is milli-Jy level. Hence, the required dynamic range can be attainable with typical/normal VLBA observations which can reach about a few times of 1000 (e.g., Perley 1999).

4.2.2. Without B -amplification

In Figure 7, we show the emission spectra for the case of high- n shell with $n_{\text{ext}} = n_{\text{torus}}$. The number density of the torus is $n_{\text{torus}} = 1 \times 10^3 \text{ cm}^{-3}$ which is based on the constraint obtained by O'Dea et al. (1984). The other values of model parameters and the observed quantities are the same as the ones in Figure 4, i.e., $L_j = 5 \times 10^{45} \text{ erg s}^{-1}$ and $B_{\text{shell}} = 0.1 \text{ mG}$ and $\epsilon_e = 0.1$.

Compared with the case of low- n shell spectra, IC component is less luminous in TeV γ -ray energy band. This is due to the frequency-peak shift of the two IC components whose seed photons are the central compact region and the fading radio lobe. This is caused by (1) the shift of $E_{e,\text{max}} \sim 10^{5.5} m_e c^2$ due to the IC cooling, and (2) decrease of the velocity which leads to the longer timescale of electron acceleration since $t_{e,\text{acc}} \propto v^{-2}$. Then, the peak of IC against seed photons from the central compact region in this case is in the Thomson regime which can be written as $h\nu_{\text{IC,max}} \approx 10^9 \text{ eV} (\frac{\gamma_{e,\text{max}}}{10^{5.5}})^2 (\frac{E_{\text{mm}}}{1 \text{ meV}})$. As for IC scattering against UV and IR seed photons, $E_{e,\text{max}} \gg 12 \text{ GeV}$ still realizes Compton regime at higher energy range.

5. IMPLICATION FOR COSMIC-RAY PROTON PRODUCTION

5.1. UHECR production in the dense plasma torus?

The origin of ultra high-energy cosmic ray (UHECR) with energies above the ankle of $\gtrsim 10^{18.5} \text{ eV}$ is still under debate (e.g., Nagano & Watson 2000; Kotera & Olinto 2011). A jet in AGN is generally expected as one of the most plausible sites for UHECR production (e.g., Takahara 1990; Rachen & Biermann 1993; Norman et al. 1995; Takami & Horiuchi 2011; Kino & Asano 2011; Murase et al. 2012). It is suggested that UHECR production at the nucleus regions of AGNs tends to cause

problems due to various energy loss processes (e.g., Pe’er et al. 2009; Pe’er and Loeb 2012). Therefore, it is worthwhile discussing a new possibility away from the central nucleus regions of AGNs.

Since higher value of B -fields can be expected if B -field amplification process is in action in dense environments, here we discuss a feasibility of UHECR production in high- n shells for the first time. For simplicity, (1) we assume the standard diffusive shock acceleration (e.g., Blandford and Eichler 1987), and (2) we neglect the possible existence of heavy nuclei. It is well known that the maximum accessible energy of UHECRs ($E_{p,\max}$) is governed by both the confinement condition and energy-loss/escape condition (e.g., Kotera and Orinto 2011 and references therein).

The Larmor radius of UHECRs ($r_L \equiv E_p/eB_{\text{shell}}$) should be smaller than the shell width i.e., $r_L \lesssim \delta R_\perp$. The typical r_L for high- n fossil shell is given by

$$r_L \approx 0.13 \text{ pc} \left(\frac{E_p}{2 \times 10^{18} \text{ eV}} \right) \left(\frac{B_{\text{shell}}}{17 \text{ mG}} \right)^{-1}, \quad (12)$$

or equivalently,

$$E_p \leq E_{p,\max} \approx 2 \times 10^{18} \text{ eV} \left(\frac{\delta R_\perp}{0.13 \text{ pc}} \right) \left(\frac{B_{\text{shell}}}{17 \text{ mG}} \right)^{+1} \quad (13)$$

where we use $\delta R_\perp \sim 1.6 \text{ pc}/12 \approx 0.13 \text{ pc}$. Essentially, the confinement condition governs the maximum energy of the UHECR ($E_{p,\max}$).

The acceleration timescale of protons ($t_{p,\text{acc}}$) generally satisfies $t_{p,\text{acc}} \lesssim \min[t, t_{\text{diff}}, t_{\text{loss}}]$ where t_{diff} and t_{loss} are an diffusive escape timescale of UHECRs from the acceleration region and an energy-loss timescale of UHECRs in the acceleration region, respectively (e.g., Norman et al. 1995).

The acceleration timescale of protons at the high- n fossil shell in the coasting phase is given by

$$t_{p,\text{acc}} = 0.42 \text{ yr} \left(\frac{E_p}{2 \times 10^{18} \text{ eV}} \right) \left(\frac{B_{\text{shell}}}{17 \text{ mG}} \right)^{-1} \xi_p, \quad (14)$$

where ξ_p is the gyro-factor for proton accelerations at the shell.

Following the study of Gabici et al. (2009), we adopt the diffusion coefficient (Eq. (13)) as $D_p = 1 \times 10^{28} \chi \left(\frac{E_p}{10^{10} \text{ eV}} \right)^{1/2} \left(\frac{B}{3\mu\text{G}} \right)^{-1/2} \text{ cm}^2 \text{ s}^{-1}$ where χ is a parameter which expresses deviations from the average Galactic diffusion coefficient. The value of χ is highly uncertain. The case of $\chi = 1$ is identical to the case of the diffusion in Galactic interstellar medium. The case $\chi < 1$ accounts for a possible suppression. The value of χ will depend on the power spectrum of magnetic field turbulence (e.g., Gabici et al. 2009 and reference therein). Then, a typical diffusion timescale of the UHECRs can be estimated as $t_{\text{diff}} = \frac{\delta R_\perp^2}{6D_p} \approx 4.7 \times 10^{-4} \text{ yr} \left(\frac{\delta R_\perp}{0.13 \text{ pc}} \right)^2 \chi^{-1} \left(\frac{E_p}{2 \times 10^{18} \text{ eV}} \right)^{-1/2} \left(\frac{B_{\text{shell}}}{17 \text{ mG}} \right)^{1/2}$ (Eq. (3) in Gabici et al. 2009). In order to satisfy the condition of $t_{p,\text{acc}} \leq t_{\text{diff}}$, the value of $\chi \sim 10^{-3}$ is required. Although little is known about χ in AGN torus, highly turbulent condition in AGN torus of magneto-ionized gas is expected (e.g., Wada et al. 2002). Thus, a much slower

diffusion compared with the ordinary interstellar medium could be realized because of turbulence in the torus.

It is readily found that t_{loss} is not competitive to $t_{p,\text{acc}}$. The timescales of proton synchrotron and pp collisions are given by

$$t_{p,\text{syn}} \approx 2.5 \times 10^5 \text{ yr} \left(\frac{B_{\text{shell}}}{17 \text{ mG}} \right)^{-2} \left(\frac{E_p}{2 \times 10^{18} \text{ eV}} \right)^{-1} \quad (15)$$

and

$$t_{pp} \approx 5 \times 10^4 \text{ yr} \left(\frac{n_{\text{shell}}}{10^3 \text{ cm}^{-3}} \right)^{-1}, \quad (16)$$

respectively. These are significantly longer than $t_{p,\text{acc}}$. Therefore, we conclude that the high- n shell can be a candidate of CR generator at least up to $\sim 2 \times 10^{18} \text{ eV}$.

5.2. The case in shocks in circum-nuclear matter

What about a further possibility of production of UHECRs in such high- n shells up to $\sim 10^{20} \text{ eV}$ in circum-nuclear matter which extends at larger scale? Here, we briefly discuss it.

Schwachter et al. (2013) reported the existence of the molecular hydrogen accretion flow in the inner 50 pc of NGC1275 by the Gemini North telescope observation. The accretion flow is oriented perpendicular to the radio jet axis. They interpret it as the outer part of a collisionally excited turbulent accretion flow with a number density of electron of $\sim 4 \times 10^3 \text{ cm}^{-3}$. If a strong shock drives this turbulent hydrogen accretion flow, then a geometrically thick shell with its width $\delta R \sim 5 \text{ pc}$ is expected. Then, such high- n shells could produce UHECRs with the energy of a few $\times 10^{19} \text{ eV}$ together with the assumption that the B -field strength is averaged by turbulence in the hydrogen accretion flow. However, it seems natural to suppose that B -field strength and the shock propagation velocity may decrease at large scale. Therefore, it is not clear whether the molecular hydrogen accretion flow observed by Schwachter et al. (2013) is really a good site for producing UHECRs.

So far, we conservatively adopt the Berezhko’s amplification factor (Berezhko 2008). However, some previous work seems to indicate higher amplification rate of the B -fields. For example, Fraschetti (2013) examined the magnetic field amplification driven by the motion of vortical eddies and the amplification factor of the field can reach $\sim 10^3$ using reasonable parameters. If this is the case in 3C 84, then there is a possibility of production of UHECRs up to $\sim 10^{20} \text{ eV}$.

6. SUMMARY

In the present work, we explored the physical properties of a fossil shell associated with fading radio lobe in 3C 84. In our recent work presented in I15, we have modeled the dynamical and spectral evolution of fossil shells that are identical to the forward shocks propagating in the external medium and found that the fossil shell emission overwhelms the fading radio lobe after the injection of energy and fresh particles from the jet has swathed off. In fact, the forward shock still continues to supply fresh electrons into the shell, while the radio lobe rapidly fades away. We apply this model to 3C 84. Below we summarize the results.

- The low- n fossil shell made of shocked ambient matter with the number density of $\sim 0.3 \text{ cm}^{-3}$ shows IC-dominated spectrum and it can be compatible to the sensitivity of CTA. Presumable TeV γ -ray emission from the central compact region may compete with the fossil shell emission. The brightness of TeV γ -ray depends on the activity of the central compact region in which blazar region is included. Hence we need to choose a low-activity phase of the blazar region for exploring the fossil shell emission in TeV γ -ray band. The predicted radio emission from this low- n fossil shell is much below the typical sensitivity of VLBI.
- The high- n shell made of shocked torus with the density of $\sim 10^3 \text{ cm}^{-3}$ shows a brighter synchrotron spectrum in general peaking at higher frequency and reaching a higher luminosity than in the case of a low- n fossil shell. In particular, if magnetic field amplification is effective in the high- n shell, then the field strength conservatively reaches $\sim 17 \text{ mG}$ order. Interestingly, the theoretical prediction of this fossil shell and detection threshold at radio band is comparable in this case. Hence, performing VLBI observations with higher dynamic range is important for a first detection of fossil shell with high- n .
- We propose that the high- n shell with B -fields amplification is a possible site for UHECRs. The predicted $E_{p,\text{max}}$ in the high- n shell in 3C 84 is about $2 \times 10^{18} \text{ eV}$ when a slow diffusion in the plasma torus takes place. The value of $E_{p,\text{max}}$ is proportional to the B -field strength, which is determined by non-linear process of field amplification. If the field amplification factor in 3C 84

is higher than that derived by Berezhko (2008), which is suggested by Frascchetti (2013), then 3C 84 can be a possible site for UHECR with the energy $\sim 10^{20} \text{ eV}$.

- An actual spectrum should be the sum of high- n and low- n shells. Therefore, cooperative observations between VLBI and CTA would be more effective and highly encouraged for exploring physical properties of the fossil shells in 3C 84 in great detail.

Acknowledgment

We thank the anonymous referee for the review and suggestions for improving the paper. We sincerely thank M. Orienti for fruitful discussions and useful comments. This research has made use of data from the MOJAVE database that is maintained by the MOJAVE team (Lister et al. 2009). The VLBA is operated by the US National Radio Astronomy Observatory (NRAO), a facility of the National Science Foundation operated under cooperative agreement by Associated Universities, Inc. This work is partly based on observations made with the KaVA, which is operated by the Korea Astronomy and Space Science Institute (KASI) and the National Astronomical Observatory of Japan (NAOJ). Data analysis was in part carried out on PC cluster and computers at Center for Computational Astrophysics, NAOJ. HI acknowledges the financial support of a Grant-in-Aid for Young Scientists (B:16K21630). NK acknowledges the financial support of Grant-in-Aid for Young Scientists (B:25800099). HN is supported by MEXT KAKENHI Grant Number 15K17619. Part of this work was done with the contribution of the Italian Ministry of Foreign Affairs and University and Research for the collaboration project between Italy and Japan.

REFERENCES

- Abdo, A. A., Ackermann, M., Ajello, M., et al. 2009, *ApJ*, 699, 31
- Ahnen, M. L., Ansoldi, S., Antonelli, L. A., et al. 2016, *A&A*, 589, A33
- Aleksić, J., Ansoldi, S., Antonelli, L. A., et al. 2014, *A&A*, 564, A5
- Asada, K., Kameno, S., Shen, Z.-Q., et al. 2006, *PASJ*, 58, 261
- Achterberg, A., Gallant, Y. A., Kirk, J. G., & Guthmann, A. W. 2001, *MNRAS*, 328, 393
- Bednarz, J., & Ostrowski, M. 1998, *Physical Review Letters*, 80, 3911
- Berezhko, E. G. 2008, *ApJ*, 684, L69
- Begelman, M. C., Blandford, R. D., & Rees, M. J. 1984, *Reviews of Modern Physics*, 56, 255
- Bell, A. R., & Lucek, S. G. 2001, *MNRAS*, 321, 433
- Blandford, R., & Eichler, D. 1987, *Phys. Rep.*, 154, 1
- Calderone, G., Sbarrato, T., & Ghisellini, G. 2012, *MNRAS*, 425, L41
- Chida, H., Nagai, H., Akiyama, K., et al. 2014, *Proceedings of the 12th European VLBI Network Symposium and Users Meeting (EVN 2014)*, 73
- Carilli, C. L., Perley, R. A., & Dreher, J. H. 1988, *ApJ*, 334, L73
- Coppi, P. S., & Aharonian, F. A. 1997, *ApJ*, 487, L9
- Czerny, B., & Hryniewicz, K. 2011, *A&A*, 525, L8
- Franceschini, A., Rodighiero, G., & Vaccari, M. 2008, *A&A*, 487, 837
- Fabian, A. C. 2012, *ARA&A*, 50, 455
- Fabian, A. C., Sanders, J. S., Taylor, G. B., et al. 2006, *MNRAS*, 366, 417
- Frascchetti, F. 2013, *ApJ*, 770, 84
- Fujita, Y., Kohri, K., Yamazaki, R., & Kino, M. 2007, *ApJ*, 663, L61
- Fujita, Y., Kawakatu, N., Shlosman, I., & Ito, H. 2016, *MNRAS*, 455, 2289
- Fujita, Y., & Nagai, H. 2017, *MNRAS*, 465, L94
- Gabici, S., Aharonian, F. A., & Casanova, S. 2009, *MNRAS*, 396, 1629
- Ghisellini, G., Tavecchio, F., Maraschi, L., Celotti, A., & Sbarrato, T. 2014, *Nature*, 515, 376
- Giacalone, J., & Jokipii, J. R. 2007, *ApJ*, 663, L41
- Greene, J. E., & Ho, L. C. 2005, *ApJ*, 630, 122
- Guo, F., Li, S., Li, H., et al. 2012, *ApJ*, 747, 98
- Gupta, M., Sikora, M., & Nalewajko, K. 2016, *MNRAS*, 461, 2346
- Heinz, S., Reynolds, C. S., & Begelman, M. C. 1998, *ApJ*, 501, 126
- Ho, L. C., Filippenko, A. V., Sargent, W. L. W., & Peng, C. Y. 1997, *ApJS*, 112, 391
- Inoue, T., Yamazaki, R., & Inutsuka, S.-i. 2009, *ApJ*, 695, 825
- Ito, H., Kino, M., Kawakatu, N., & Orienti, M. 2015, *ApJ*, 806, 241 (I15)
- Ito, H., Kino, M., Kawakatu, N., & Yamada, S. 2011, *ApJ*, 730, 120
- Ji, S., Oh, S. P., Ruszkowski, M., & Markevitch, M. 2016, *MNRAS*, 463, 3989
- Kameno, S., Sawada-Satoh, S., Inoue, M., Shen, Z.-Q., & Wajima, K. 2001, *PASJ*, 53, 169
- Kawabata, K. S., Nagae, O., Chiyonobu, S., et al. 2008, *Proc. SPIE*, 7014, 70144L
- Kawakatu, N., Kino, M., & Nagai, H. 2009a, *ApJ*, 697, L173

| TABLE 1 PHYSICAL QUANTITIES IN 3C84 | | | | |
|---|--------------------|---|--|--|
| quantities | symbols | values | note | |
| Eddington power | L_{Edd} | 1×10^{47} ergs s^{-1} | Scharwachter et al. (2013) | |
| jet power | L_{j} | 5×10^{45} ergs s^{-1} | Heinz et al. (1998) | |
| age of dying radio lobe | t | 50 – 60 years | in 2015, Nesterov et al. (1995) | |
| number density of ambient medium | n_{amb} | 0.3 cm^{-3} | Fabian et al. (2006) | |
| power-law index of ambient medium | α | 0 | Eq. (1), flat | |
| number density of plasma torus | n_{torus} | $1 \times 10^3 \text{ cm}^{-3}$ | O’Dea et al. (1984) | |
| radius (in 2015) | R_{\parallel} | 9.3 – 16.6 pc | Tavecchio et al. (2014); Fujita & Nagai (2016) | |
| propagation velocity | v_{\parallel} | 0.3 – 0.5 c | Asada et al. (2006), Lister et al. (2013) | |
| UV luminosity (accretion disk) | L_{UV} | 5×10^{42} ergs s^{-1} | KANATA | |
| IR luminosity (dust torus) | L_{IR} | $L_{\text{UV}}/2$ | Calderone et al. (2012) | |
| Radio luminosity (central compact region) | $L_{43\text{G}}$ | 4×10^{42} ergs s^{-1} | Fig. 3 | |
| Radio luminosity (central compact region) | $L_{22\text{G}}$ | 2×10^{42} ergs s^{-1} | VERA (Chida et al. 2015) | |
| Radio luminosity (fading radio robe) | L_{lobe} | 1×10^{41} ergs s^{-1} | Fig. 2 | |

| TABLE 2 MODEL PARAMETERS | | | | | |
|---|-------------------------------------|--|---|---|------|
| quantities | symbols | low- n | high- n w/o B -amp | high- n w/ | |
| number density of external matter | n_{ext} | $n_{\text{ext}} = n_{\text{amb}} = 0.3 \text{ cm}^{-3}$ | $n_{\text{ext}} = n_{\text{torus}} = 1 \times 10^3 \text{ cm}^{-3}$ | $n_{\text{ext}} = n_{\text{torus}} = 1$ | |
| magnetic field in the shell | B_{shell} | 0.1mG | 0.1mG | | 17mG |
| fraction of non-thermal electrons | $\epsilon_{\text{e,shell}}$ | 0.1 | 0.1 | | 0.01 |
| power-law index of injected electrons | p_{shell} | 2 | 2 | | 2 |
| electron gyro-factor | ξ_{shell} | 10 | 10 | | 10 |
| volume filling factor in the shell | $f_{\text{amb}} = f_{\text{torus}}$ | 0.5 | 0.5 | | 0.5 |
| Kawakatu, N., Nagao, T., & Woo, J.-H. 2009b, ApJ, 693, 1686 | | Norman, C. A., Melrose, D. B., & Achterberg, A. 1995, ApJ, 454, 60 | | | |
| Kino, M., Ito, H., Kawakatu, N., et al. 2016, Astronomische Nachrichten, 337, 47 | | O’Dea, C. P., Dent, W. A., & Balonek, T. J. 1984, ApJ, 278, 89 | | | |
| Kino, M., Ito, H., Kawakatu, N., & Orienti, M. 2013, ApJ, 764, 134 | | Ostorero, L., Moderski, R., Stawarz, L., et al. 2010, ApJ, 715, 1071 | | | |
| Kino, M., & Asano, K. 2011, MNRAS, 412, L20 | | Ostriker, J. P., & McKee, C. F. 1988, Reviews of Modern Physics, 60, 1 | | | |
| Kirk, J. G., Guthmann, A. W., Gallant, Y. A., & Achterberg, A. 2000, ApJ, 542, 235 | | Perley, R. A. 1999, Synthesis Imaging in Radio Astronomy II, 180, 275 | | | |
| Komatsu, E., Smith, K. M., Dunkley, J., et al. 2011, ApJS, 192, 18 | | Pe’er, A., & Loeb, A. 2012, JCAP, 3, 007 | | | |
| Kotera, K., & Olinto, A. V. 2011, ARA&A, 49, 119 | | Pe’er, A., Murase, K., & Mészáros, P. 2009, Phys. Rev. D, 80, 123018 | | | |
| Levinson, A., Laor, A., & Vermeulen, R. C. 1995, ApJ, 448, 589 | | Piran, T. 1999, Phys. Rep., 314, 575 | | | |
| Lister, M. L., Aller, H. D., Aller, M. F., et al. 2009, AJ, 137, 3718 | | Plambeck, R. L., Bower, G. C., Rao, R., et al. 2014, ApJ, 797, 66 | | | |
| Lister, M. L., Aller, M. F., Aller, H. D., et al. 2013, AJ, 146, 120 | | Rachen, J. P., & Biermann, P. L. 1993, A&A, 272, 161 | | | |
| Lucarelli, F., Pittori, C., Verrecchia, F., et al. 2017, The Astronomer’s Telegram, 9934 | | Reynolds, C. S., & Begelman, M. C. 1997, ApJ, 487, L135 | | | |
| Lucek, S. G., & Bell, A. R. 2000, MNRAS, 314, 65 | | Rocha da Silva, G., Falceta-Gonçalves, D., Kowal, G., & de Gouveia Dal Pino, E. M. 2015, MNRAS, 446, 104 | | | |
| Marcowith, A., Bret, A., Bykov, A., et al. 2016, Reports on Progress in Physics, 79, 046901 | | Sano, T., Nishihara, K., Matsuoka, C., & Inoue, T. 2012, ApJ, 758, 126 | | | |
| Mittal, R., Oonk, J. B. R., Ferland, G. J., et al. 2012, MNRAS, 426, 2957 | | Scharwächter, J., McGregor, P. J., Dopita, M. A., & Beck, T. L. 2013, MNRAS, 429, 2315 | | | |
| Mirzoyan, R. 2017, The Astronomer’s Telegram, 9929 | | Shepherd, M. C. 1997, Astronomical Data Analysis Software and Systems VI, 125, 77 | | | |
| Mirzoyan, R. 2016, The Astronomer’s Telegram, 9689 | | Shakura, N. I., & Sunyaev, R. A. 1973, A&A, 24, 337 | | | |
| Mukherjee, R., & VERITAS Collaboration 2017, The Astronomer’s Telegram, 9931 | | Silver, C. S., Taylor, G. B., & Vermeulen, R. C. 1998, ApJ, 502, 229 | | | |
| Mukherjee, R., & VERITAS Collaboration 2016, The Astronomer’s Telegram, 9690 | | Suzuki, K., Nagai, H., Kino, M., et al. 2012, ApJ, 746, 140 | | | |
| Murase, K., Dermer, C. D., Takami, H., & Migliori, G. 2012, ApJ, 749, 63 | | Takahara, F. 1990, Progress of Theoretical Physics, 83, 1071 | | | |
| Nagai, H., Orienti, M., Kino, M., et al. 2012, MNRAS, 423, L122 | | Takami, H., & Horiuchi, S. 2011, Astroparticle Physics, 34, 749 | | | |
| Nagai, H., Suzuki, K., Asada, K., et al. 2010, PASJ, 62, L11 | | Taylor, G. B., Gugliucci, N. E., Fabian, A. C., et al. 2006, MNRAS, 368, 1500 | | | |
| Nagano, M., & Watson, A. A. 2000, Reviews of Modern Physics, 72, 689 | | Tavecchio, F., & Ghisellini, G. 2014, MNRAS, 443, 1224 | | | |
| Nesterov, N. S., Lyuty, V. M., & Valtaoja, E. 1995, A&A, 296, 628 | | Taylor, G. B., Gugliucci, N. E., Fabian, A. C., et al. 2006, MNRAS, 368, 1500 | | | |
| Netzer, H., & Laor, A. 1993, ApJ, 404, L51 | | Walker, R. C., Dhawan, V., Romney, J. D., Kellermann, K. I., & Vermeulen, R. C. 2000, ApJ, 530, 233 | | | |
| Niinuma, K., Lee, S.-S., Kino, M., et al. 2014, PASJ, 66, 103 | | Yamazaki, S., Fukazawa, Y., Sasada, M., et al. 2013, PASJ, 65, 197 | | | |
| | | Wada, K., Meurer, G., & Norman, C. A. 2002, ApJ, 577, 197 | | | |

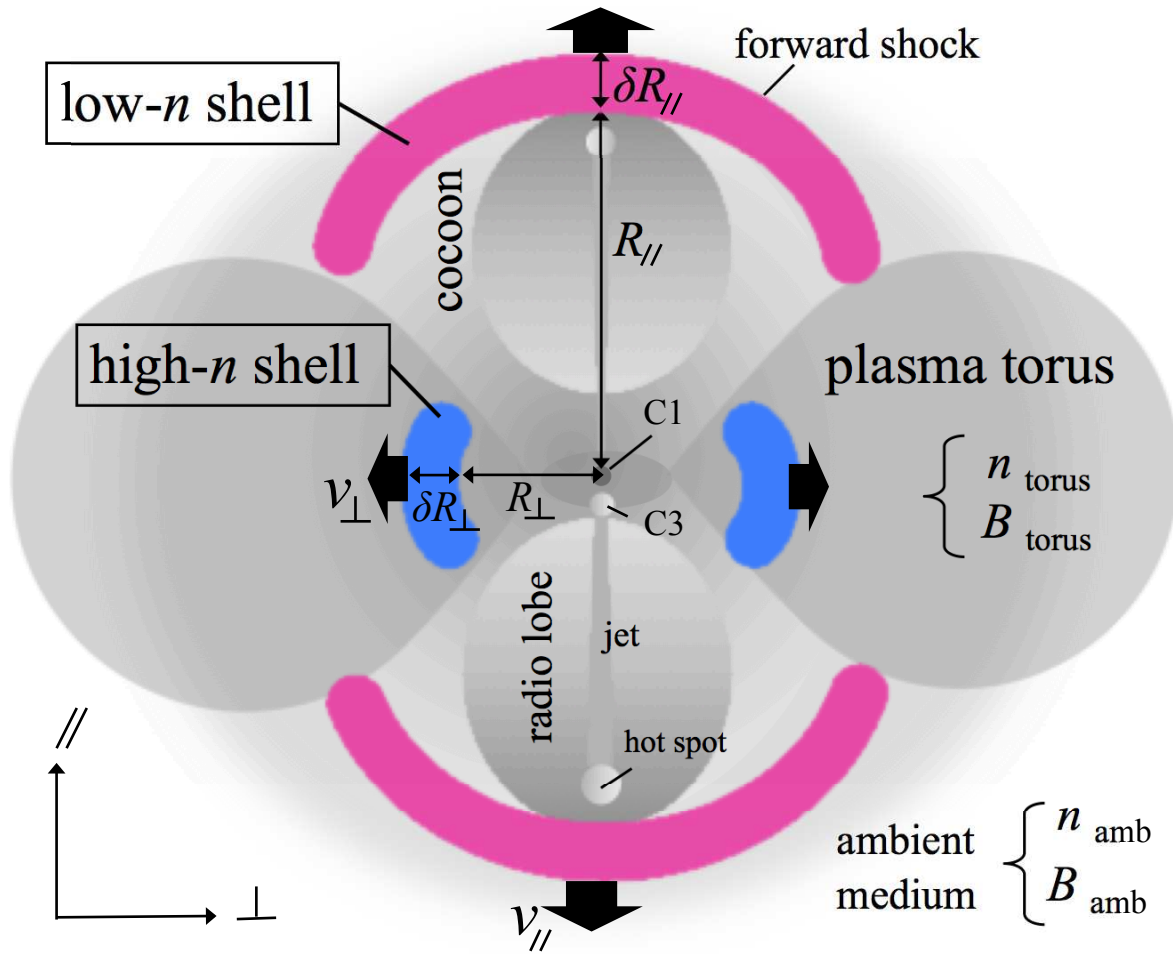


FIG. 1.— A schematic picture of the jet and external medium interaction in 3C 84. In this picture, side-on view (i.e., the jet viewing angle as 90 degree) is adopted for convenience.

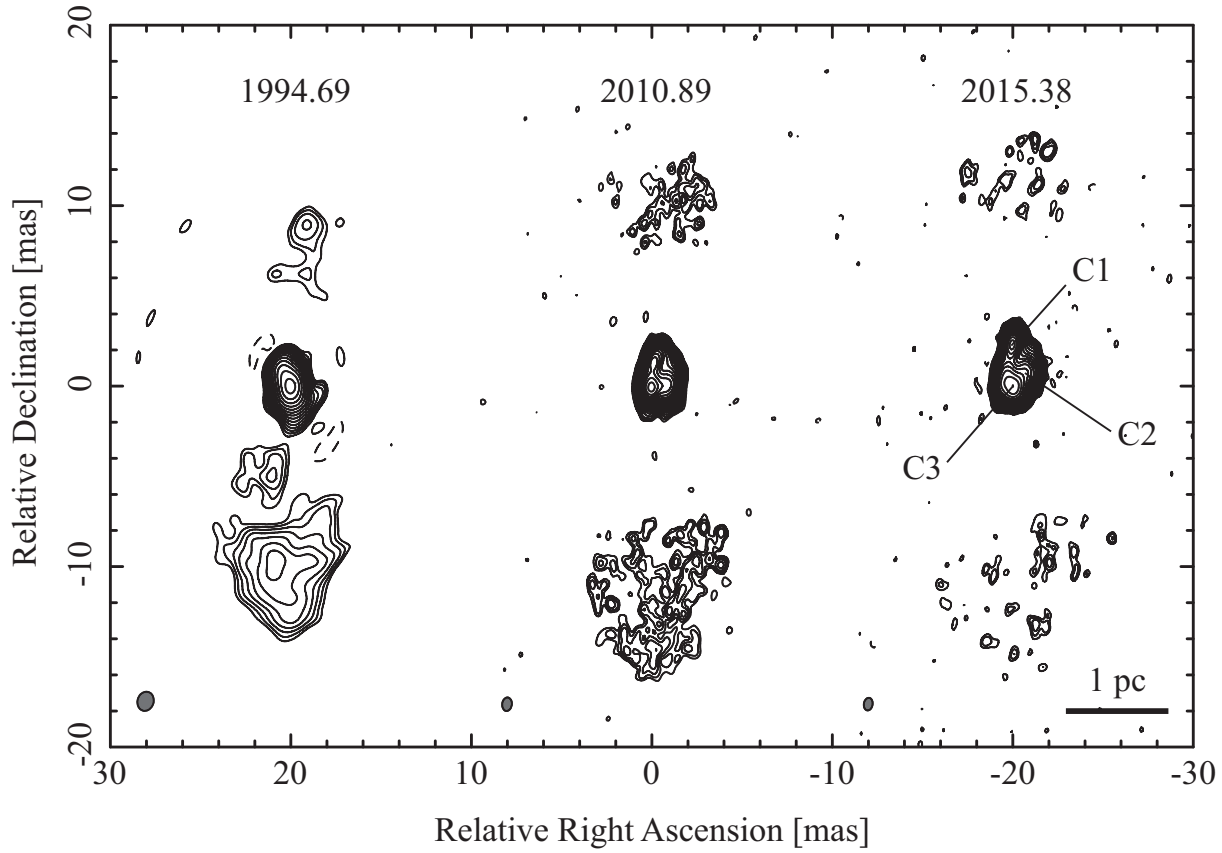


FIG. 2.— The comparison of the three epochs overall 3C 84 radio lobe images with VLBA at 15 GHz in 1994, 2010, and 2015 (data are adopted from the VLBA archival data with the project ID BR003, BL149CX, and BL193AS, respectively). The central compact lobe and a pair of fading radio lobes are seen in each epoch. The total fluxes of the northern lobe, the central compact region (composed of C1, C2 and C3 components), and the southern lobe are respectively, 0.75, 13.89, 6.66 Jy (in 1994), 0.52, 20.56, 1.44 Jy (in 2010), and 0.40, 28.06, 0.76 Jy (in 2015). Note that the brightness peak (phase-center) in the image coincides with C1 in 1994 while the peak is at C3 in 2010 and 2015. The image rms is ~ 3 mJy/beam (1σ) for the epoch in 2015.

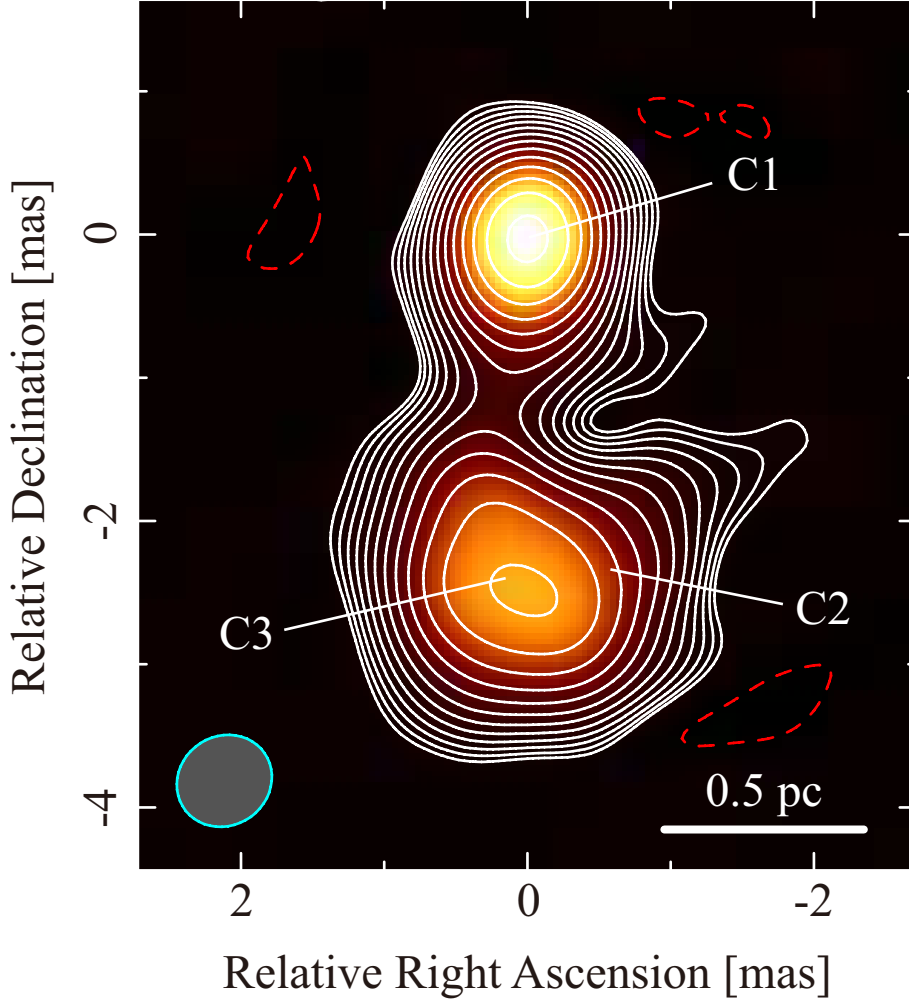


FIG. 3.— KaVA image of the central compact region in 3C 84 obtained in 2015. The map peak intensity is 5.3 Jy/beam. The synchrotron emission from the central compact region is the major seed photons for the IC scattering in the fossil shells.

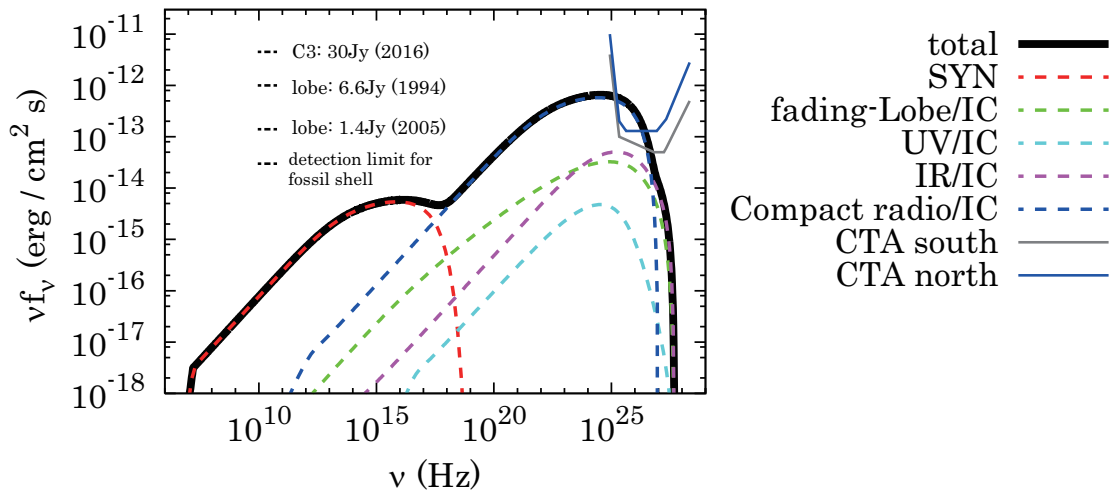


FIG. 4.— Low- n shell spectrum in 3C 84 (predicted in 2015 and evolution after that) with $n_{\text{amb}} = 0.3 \text{ cm}^{-3}$, $L_j = 5 \times 10^{45} \text{ erg s}^{-1}$, $t = 55 \text{ yr}$ and $B_{\text{shell}} = 0.1 \text{ mG}$. Further model parameter values and the observed quantities are completely summarized in Tables 1 and 2. The shell spectrum is IC-cooling dominated and the IC component of synchrotron photons from the central compact region (gray line) is dominant.

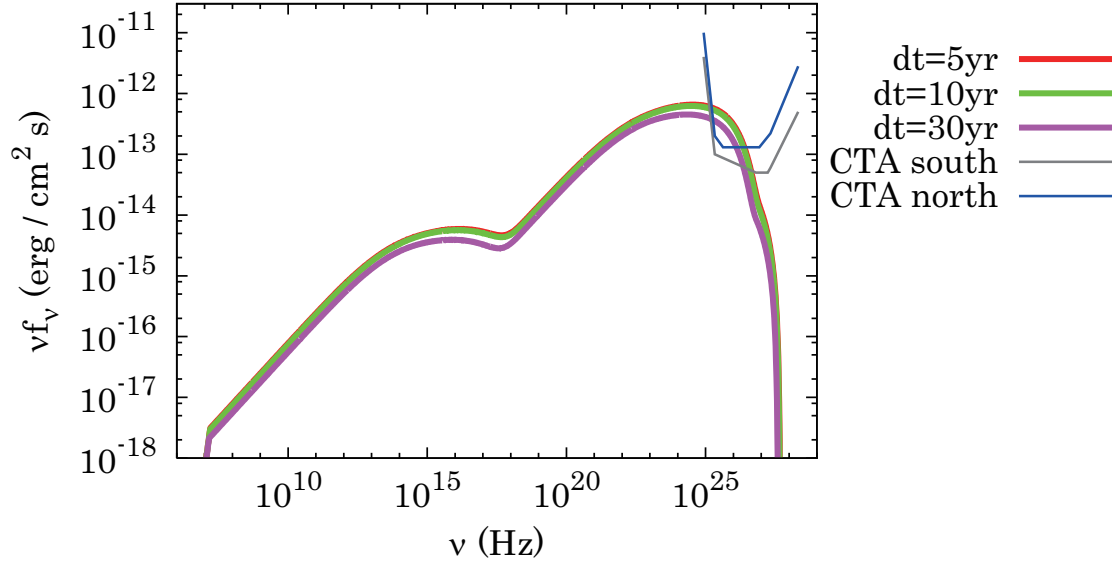


FIG. 5.— Spectral evolution of the fossil shell where $n_{\text{ext}} = n_{\text{amb}} = 0.3 \text{ cm}^{-3}$. Three epochs with the durations after the jet stopping as 5, 10 and 30 years are shown here. The spectra are almost constant in time because of continuous injection of fresh electrons in the shell via the forward shock.

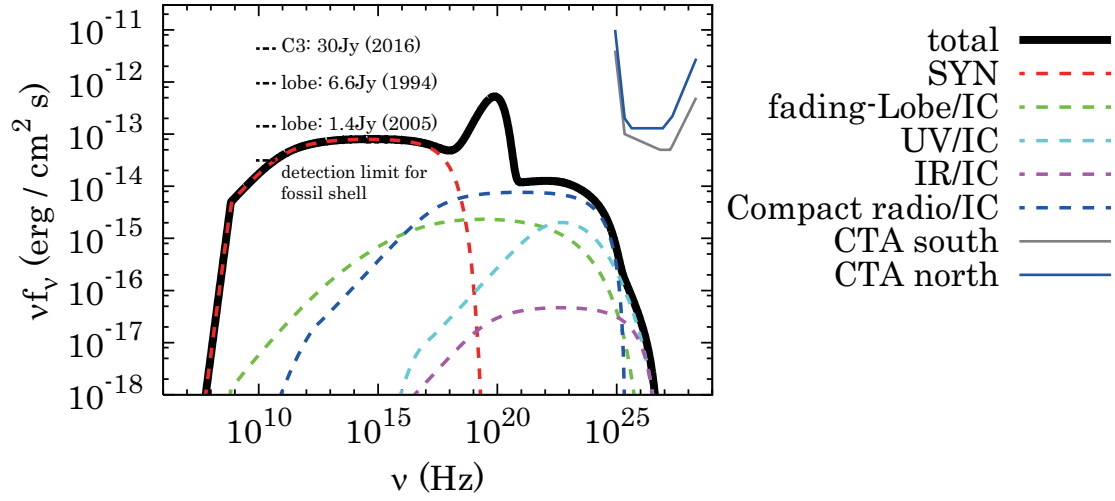


FIG. 6.— Same as Figure 4 but with $n_{\text{ext}} = n_{\text{torus}} = 1 \times 10^3 \text{ cm}^{-3}$ and B -field amplification. This case is defined as high- n shell. The bump at 10^{20} Hz corresponds to thermal bremsstrahlung emission.

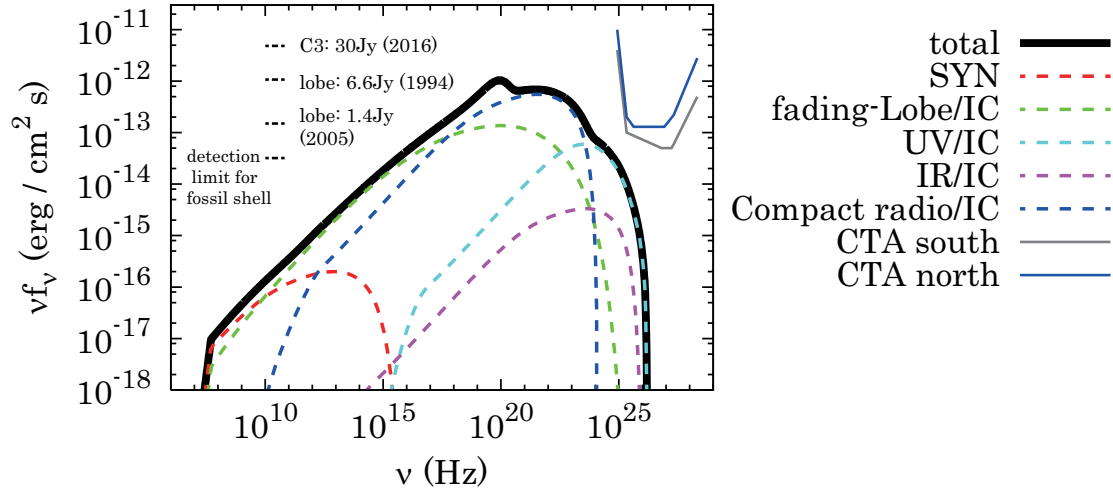


FIG. 7.— Same as Figure 4 but with $n_{\text{ext}} = n_{\text{torus}} = 1 \times 10^3 \text{ cm}^{-3}$, i.e., without B -field amplification.